Remote Sensing of Environment 157 (2015) 170–184

Contents lists available at ScienceDirect

Remote Sensing of Environment

journal homepage: www.elsevier.com/locate/rse

Time-series analysis of Landsat-MSS/TM/OLI images over Amazonian waters impacted by gold mining activities

Felipe L. Lobo [a,*], Maycira P.F. Costa [a], Evlyn M.L.M. Novo [b]

[a] Spectral Lab, Department of Geography, University of Victoria, Victoria, BC, V8W 3R4, Canada
[b] National Institute for Space Research (INPE), Remote Sensing Division, Av. dos Astronautas, 1758 - Jardim da Granja, São José dos Campos, SP-12227-010, Brazil

ARTICLE INFO

Article history:
Received 30 December 2013
Received in revised form 30 March 2014
Accepted 17 April 2014
Available online 9 July 2014

Keywords:
Landsat time-series
Atmospheric correction
Deglinting
Turbid rivers
Suspended solids
Temporal analysis
Gold mining
The Brazilian Amazon

ABSTRACT

Water siltation caused by artisanal gold mining has impacted the Tapajós River Basin in Brazil for the past 40 years, however spatial-temporal information about changes in water quality and consequences to the aquatic environment is lacking. To address this, the Landsat satellite family sensors were used to retrieve total suspended solids (TSS) of the water of the Tapajós River from 1973 to 2013. An image processing approach that includes atmospheric correction, based on the 6S model, and glint removing, based on shortwave infrared correction, was applied and validated with *in situ* radiometric data. An optimization of the atmospheric correction having dark dense forest spectra as reference was applied and allowed a robust correction of MSS, TM and OLI signal to surface reflectance values. Sediment concentration was estimated based on a non-linear empirical regression between measured TSS and satellite surface reflectance at red band. The multi-temporal analysis of TSS showed that the sediment load in the Tapajós aquatic system is in synchrony with mining activities, and a constant seasonal variation of water siltation is observed throughout the time frame of this study. At the end of the rainy season, mining activities intensify and, coupled with low water flow, TSS increases. During the high water level, TSS concentrations were consistently lower because of high water dilution and low mining activity. In a decadal analysis, a peak of sediment concentration coincides with a peak of gold production in all sites analyzed during early 1990s. More recently, due to the currently gold rush, an increase in suspended solids has been observed mainly in the Novo and Tocantins rivers where industrial mining has been installed.

1. Introduction

The Tapajós River Basin, in the Amazon Basin, has been contaminated with mercury and impacted with water siltation due to discharges of artisanal gold-mining tailings into its tributaries since 1950s (Sousa & Veiga, 2009). The artisanal mining activities expanded in the 1980s when high gold prices stimulated around 30,000 workers to extract gold in this area (Bezerra, Veríssimo, & Uhl, 1998). The activity decreased in the following decades; however, due to current high gold prices, a new gold rush is taking place not only in the Amazon, but also in many other countries (Schueler, Kuemmerle, & Schroeder, 2011; Tudesque, Grenouillet, Gevrey, Khazraie, & Brosse, 2012).

Previous studies in the Tapajós Basin (Rodrigues, 1994; Telmer, Costa, Simões Angélica, Araujo, & Maurice, 2006) reported that artisanal gold mining discharge into the rivers enormous amounts of fine inorganic sediment by removing top soil layers from the margins, and also by revolving sediment from the bottom. Because of its high scattering properties, inorganic suspended particles in the water backscatter part of the incoming light, thus reducing light availability in the water column (Kirk, 2011). Roland and Esteves (1998) have shown that an increase in suspended matter of nearly 34 mg/l in an Amazonian crystalline lake (Batata Lake) raises total light attenuation, and consequently reduces the phytoplankton density by approximately 50%. Guenther and Bozelli (2004) suggested that the decrease in phytoplankton densities recorded in Batata Lake may not be related to phytoplankton loss due to algal-clay aggregation, but rather is a consequence of decreasing growth rates because of light attenuation. The high light backscattering in turbid waters results in high water-leaving reflectance, easily detected by remote sensors as shown by Telmer and Stapper (2007) in the Tapajós River. Considering the large scale of the water siltation impact, Telmer and Stapper (2007) have indicated the potential of using remote sensing data to monitor turbidity and to investigate its consequences to the ecosystems of the Tapajós River.

Although not designed for water body studies, Landsat MSS and TM have been effectively used to estimate total suspended solids (TSS) in coastal and inland waters (Binding, Bowers, & Mitchelson-Jacob, 2005; Harrington, Schiebe, & Nix, 1992). Detection of water leaving radiance from turbid waters with high confidence is possible, first because the sensor's spatial resolution (up to 80 m on MSS) allows imaging rivers and estuarine areas, and second because of the signal-to-noise ratio of

* Corresponding author at: Department of Geography University of Victoria PO Box 3060 STN CSC, Victoria, BC, Canada V8W 3R4. Tel.: +1 778 678 2043.
E-mail address: lobo@uvic.ca (F.L. Lobo).

http://dx.doi.org/10.1016/j.rse.2014.04.030
0034-4257/

these sensors (250:1) (Dekker, Vos, & Peters, 2002). The use of these sensors for estimating suspended solids in the water generally follows two approaches: the empirical approach, which relies on direct correlation between measured TSS and satellite data (Hadjimitsis & Clayton, 2009; Mertes, Smith, & Adams, 1993); or analytical methods, which rely on measured water optical properties (Albert & Mobley, 2003; Doxaran et al., 2012). These studies show that green and red bands correlate well with TSS up to approximately 100 mg/l. Under higher concentrations, however, these bands saturate and NIR bands present a better predictor of TSS (Wang, Lu, Liew, & Zhou, 2009).

Given the recently launched OLI (Operational Land Imager) sensor on board Landsat-8, with similar characteristics of a TM sensor, the capability of using time series based on Landsat imagery for evaluation of temporal changes and monitoring purposes is extended to the present; a time series of 40 years (1973–2013) of Landsat imagery is currently available. However, given differences in the sensor's resolution and in atmospheric conditions at the time of imagery acquisition, a proper comparison between water leaving signals requires that all images have to be corrected for atmospheric effects and normalized to reference images or reference targets (Hadjimitsis & Clayton, 2009). Most of the images from the study area present at least 40% cloud cover. Atmospheric correction would be necessary to minimize the atmospheric effects on historical Landsat images that are not validated with *in situ* measurements.

This paper has a threefold objective: (i) define an image processing procedure that corrects Landsat digital numbers (DN) to surface reflectance ($\rho_{surf}(\lambda)$), allowing inter-comparison between Landsat data from 1973 (MSS) to 2013 (OLI); (ii) apply the procedure to build a reliable time series of water surface reflectance to retrieve TSS concentration from historical images in the Tapajós River Basin; (iii) use the retrieved suspended sediment concentrations for temporal and spatial analysis of sediment changes and gold mining activity in the Tapajós River Basin.

2. Theoretical background

2.1. Atmospheric effects and correction methods

When sensing a water body, the measured radiance, $L_{total}(\lambda)$, is the sum of the target radiance and radiance from atmospheric attenuation:

$$L_{total}(\lambda) = L_{path}(\lambda) + t \cdot L_{target}(\lambda) \quad (1)$$

where $L_{path}(\lambda)$ stands for radiance scattered by the atmosphere given a wavelength (λ), t is the diffuse transmittance from the target to the sensor and $L_{target}(\lambda)$ is the upwelling radiance from the water body.

Depending on the atmospheric conditions, more than 80% of the total signal can be attributed to atmospheric scattering processes (Albert & Mobley, 2003; Hu, Muller-Karger, Andrefouet, & Carder, 2001). Note that the total radiance, $L_{total}(\lambda)$, can also include the surface reflection of the direct solar beam, $L_{glint}(\lambda)$, and, in shallow waters, the effect of light reflected from the bottom, $L_{bottom}(\lambda)$.

$$L_{total}(\lambda) = L_{path}(\lambda) + L_{glint}(\lambda) + t \cdot L_{bottom}(\lambda) + t \cdot L_{target}(\lambda) \quad (2)$$

Eq. (2) is often normalized to incidental light to yield a dimensionless reflectance term, $\rho_{TOA}(\lambda)$ (Gordon & Wang, 1994):

$$\rho_{TOA}(\lambda) = \pi \cdot L_{total}(\lambda)/E_o \cdot cos\theta_0 \quad (3)$$

where E_o is the top of atmosphere (TOA) solar irradiance and $\theta_0$is the solar zenith angle.

In order to correct $\rho_{TOA}(\lambda)$ to $\rho_{surf}(\lambda)$, atmospheric correction on Landsat-TM data over inland waters has been carried out using radiative transfer models (physically based), such as Lowtran and 6S, because of accurate outputs when local atmospheric conditions are known (Gong, Huang, Li, & Wang, 2008). This method requires information about atmospheric conditions to model the effects and remove them from the sensor's signal. According to the 6S model, surface reflectance (ρ_{surf}) is derived from the following equation (Vermote, Tanre, Deuze, Herman, & Morcette, 1997):

$$\rho_{TOA} = t_{gas}(O_3, O_2) \times \left[\rho_{r+a} + t_{H2O} \cdot t_{r+a} \cdot \rho_{surf}\right] \quad (4)$$

where ρ_{TOA} is the TOA reflectance; ρ_{r+a}, Rayleigh and aerosol reflectance; t_{r+a}, Rayleigh and aerosol transmittance; $t_{gas}(O_3, O_2)$, gases transmittance; and t_{H2O}, water vapor transmittance.

The 6S model provides pre-defined atmosphere conditions to be chosen according to scene location and altitude, atmospheric type, and relative humidity, to accommodate the common lack of input data about *in situ* gases and aerosol concentrations (Vermote et al., 1997). For the Brazilian Amazon, for example, tropical atmospheric and continental aerosol conditions are commonly used (Lu, Mausel, Brondizio, & Moran, 2002).

Besides atmospheric effects, surface specular reflectance, commonly called glint, has to be considered for deriving accurate water reflectance (Hedley, Harborne, & Mumby, 2005). The deglinting procedure as described by Hochberg, Andrefouet, and Tyler (2003) and Hedley et al. (2005) relies on two simple assumptions: (1) that the brightness in the infra-red is composed only of sun glint; and (2) that the amount of sun glint in the visible bands is linearly related to the brightness in the NIR band. The use of NIR for deglinting signal from turbid waters may overcorrect the visible bands (Le, Li, Zha, Sun, & Yin, 2009) because it can present considerable signal (up to 5%) when TSS is up to 25.0 mg/l, as an example given by Bale, Tocher, Weaver, Hudson, and Aiken (1994). For that reason, Wang and Shi (2007) suggest the SWIR band (1600 nm), which is less affected or not affected by sediment-rich water bodies, to correct the VNIR bands from glinting effect by simple subtraction:

$$\rho_{deglint}(VNIR) = \rho_{surf}(VNIR) - \rho_{surf}(SWIR) \quad (5)$$

2.2. Time-series for changes detection

The potential to use temporal series of satellite images to detect changes in surface water quality has been demonstrated, for example, by Dekker, Vos, and Peters (2001) and Wang, Xia, Fu, and Sheng (2004). For an absolute multi-temporal analysis (i.e., detected changes have to attribute solely to variation on target`s signal), one has to perform radiometric correction (including atmospheric correction) followed by normalization of the images (Hadjimitsis & Clayton, 2009; Moran et al., 2001). Normalization between images requires an application of histogram matching based on the signal from pseudo-invariant targets within the image. The assumption is that the spectra of these targets do not change over time and are therefore used to equalize histogram images (Moran et al., 2001). The pseudo-invariant targets commonly used are concrete, sand and barren lands as highly reflective targets (Puttonen, Suomalainen, Hakala, & Peltoniemi, 2009), and water bodies as dark targets. However, concrete and barren lands are often not available for the study area, and using water bodies as dark objects can compromise the absolute surface reflectance of the water bodies of interest.

As an alternative to histogram matching (Liew, Saengtuksin, & Kwoh, 2009), an absolute atmospheric correction method is proposed based on the assumption that dense dark vegetation (DDV) is considered a spectrally invariant target, and can be used as a reference target to optimize atmospheric correction. This method was established having Amazonian dark dense forest spectra as reference targets, including spectra from the Tapajós area (Liew et al., 2009), and postulates the relation, $\rho_{surf}(blue) = 0.33 * \rho_{surf}(SWIR)$, to estimate surface reflectance for the visible bands. Comparing the calculated ρ_{surf} to the TOA reflectance, aerosol optical thickness (AOT) can be estimated directly from the imagery. Masek et al. (2006) show that AOT derived from Landsat

TM imagery is highly correlated to *in situ* AOT measurements, and confirm the application of DDV as reference targets to optimize atmospheric correction for a multi-temporal analysis of ρ_{surf}.

3. Study area

The Tapajós River Basin covers more than 200,000 km^2 (Fig. 1) in the center of the Brazilian Amazon. It drains lixiviated old rocks (>2000 million years, Pre-Cambrian) which results in a naturally clear water system with low amounts of sediments and dissolved matter (Junk, 1997). For example, Costa, Novo, and Telmer (2013) reported TSS up to 5.0 mg/l in the mouth of the Tapajós River as opposed to the sediment-rich (whitewater) Amazon River that shows TSS up to 150 mg/l during water receding periods. Colored-dissolved organic matter (CDOM at 440 nm) is also low (up to 2.1 m^{-1}) when compared to CDOM-rich (blackwater) rivers such as the Negro (up to 10.7 m^{-1}) (Costa et al., 2013). Therefore, because of its natural clear water and better light conditions, phytoplankton production in the Tapajós River can be considerably greater than in whitewater and blackwater (Costa et al., 2013; Junk, 1997). The large mouth-bays of the Tapajós, for example, collect nutrients that, along with relatively good light penetration, support seasonal phytoplankton blooms (Novo et al., 2006). Costa et al. (2013) reported a seasonal variation on chlorophyll-*a* concentration (*chl-a*) from 2.1 μg/l at the receding water period to 16.3 μg/l during the ebbing season at Santarém area (see Fig. 1). The variability of the optically active components (OAC), such as TSS, *chl-a* and CDOM, can influence ρ_{surf} because of their inherently different absorption and scattering properties (Mobley, 1994). TSS is a highly-scattering component, whereas *chl-a* and CDOM are characterized by high absorption properties in the visible spectra range. The combination of absorption and scattering properties of the OAC defines the ρ_{surf} (Gordon & Brown, 1975).

The hydrological regime in the Tapajós River is very consistent over the years (Fig. 1b), and is an important factor in the biogeochemical dynamic of the water. The water reaches the highest level (March to May) at the end of the rainy season, and the lowest level during the low water season (from September to November), with a difference of 6.0 m on average. For consistency throughout the document, the high water level season refers to the period between March and May, and low water level season refers to the period between August and November (Fig. 1b). The only upstream site (Itaituba City region, see Fig. 1) that has long term sampling for TSS estimation by the Brazilian Water Agency (ANA, 2013) shows that concentration reached almost 30 mg/l in the early 1990s and dropped to a range between 5 and 12 mg/l in the following years for both seasons (Fig. 1c).

The Tapajós River Basin represents one of the largest gold reserves in the world, and since the creation of the Gold Mining District in 1983, this area has been intensively mined. Gold production reached a maximum of 22.0 tons per year in 1992 (12.5% of Brazil's total production that year) (Sousa & Veiga, 2009). In the same period, a north–south highway (BR-163) was established to connect Santarém to Cuiabá in order to support territory colonization and agriculture activities. As a result, large deforested areas along the highway can be observed, mainly at the Jamanxim sub-basin (Fig. 1). Deforestation areas are also observed around Santarém and Itaituba cities and in the Gold Mining District as a consequence of mining settlements in the area.

Gold-mining in this area is traditionally performed either by using water-jets to remove top soil layers, or by using small boats called

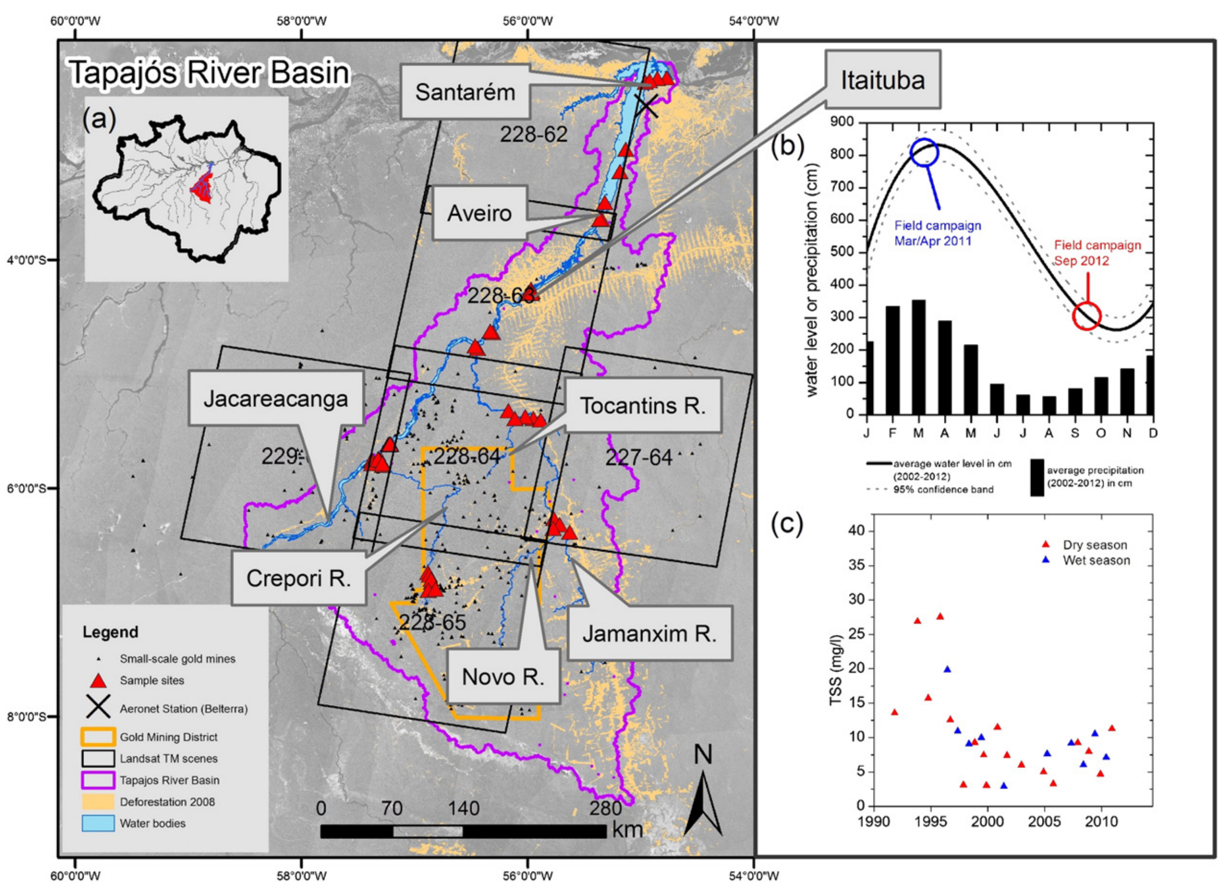

Fig. 1. (a) Location of the Tapajós River Basin in the Brazilian Amazon with indication of the main water bodies, sample sites (see Section 4.1), Aeronet station (Belterra), deforestation (INPE, 2011), gold-mining district, mines (CPRM, 2009), and Landsat TM scenes. (b) Hydrological and precipitation regime of the Tapajós River at Itaituba gauge station (center of 228/63 scene) for the past 10 years, periods of field campaigns are also shown. (c) Historical (1992–2011) TSS concentration in the Tapajós River-Itaituba City area. (Source for (b) and (c): ANA-Brazilian National Agency for Water Resources 2013.)

'balsas' that take the sediment from the bottom of the rivers using suction and separate the gold by gravity (Araújo Neto, 2009; Telmer et al., 2006). Both techniques discharge large concentrations of fine sediment into the main tributaries (Crepori, Jamanxim, and Tocantins) that can be measured kilometres downstream (Telmer et al., 2006). According to Bezerra et al. (1998), a total of 67.0 million m^3/year of sediment have been removed from the margins of many tributaries of the Tapajós River in the 1980s due to gold mining activities. Furthermore, Telmer et al. (2006) showed that the sediment plume generated during mining operations is composed mostly of fine inorganic particles that can carry significant amounts of mercury, which is used in the amalgamation process. Telmer et al. (2006) also demonstrate the applicability of monitoring the sediment plume using Landsat TM data, and indicate that satellite imagery shows great promise to be used as a modern monitoring system given the large and remote area.

4. Methods

Three main steps were conducted in order to define an image processing method for Landsat data that allows multi-temporal analysis of water surface reflectance and suspended solids in Tapajós River Basin (Fig. 2): 1) field campaigns for *in situ* radiometric and TSS data collection (box (a) in Fig. 2); 2) atmospheric correction of historical Landsat imagery based on reference images that were validated with *in situ* radiometric data (boxes (b), (c), and (d) in Fig. 2); and 3) seasonal and decadal analysis of $\rho_{surf}(\lambda)$ and suspended solids (TSS) in the Tapajós River Basin (box (e) in Fig. 2).

4.1. Radiometric and TSS data

Two field campaigns were conducted in the Tapajós River Basin to measure radiometric quantities and TSS concentrations: March/April 2011, during high water level (23 sample points); and September 2012, during low water level (16 sample points) (see Fig. 1 for sample point locations). The field campaigns were defined based on periods when the water system is less dynamic and changes in water quality are slower compared to receding or flooding periods. This choice would contribute to matching *in situ* data with concurrent satellite images. It would also help with the inter-annual comparison between images. The sample point locations were defined in order to cover the spatial distribution on the main Tapajós River tributaries before and after their discharge, and along the Tapajós River to cover its lengthwise variation.

For each sample point, two water samples were taken at a depth of 0.3 m to determine TSS concentrations according to the gravimetric method (APHA, 2005). For each water sample taken, triplicates of pre-weighted (0.7 μm) filters were used to determine TSS average and standard deviations in the laboratory. By doing so, a total full precision of TSS estimation is achieved by accounting for variability of filtering methods, and for heterogeneity of water samples.

To determine the *in situ* surface reflectance, above-water downward irradiance (E_s), and a continuous depth profile of in-water upwelling radiance, L_u, were measured using Satlantic Hyper Pro (Satlantic Inc.). These optical sensors measure hyperspectral quantities in the interval from 396 to 800 nm with 10 nm resolution. The raw data were calibrated to sensor specification, corrected for tare conditions and binned to depth intervals. In order to minimize the wave focusing/defocusing effect (Hedley et al., 2005), and uncertainties attributed to the L_u sensor tilt, triplicate measurements were taken at each sample point, and signals measured with a tilt higher than 15° were removed from the dataset. After being corrected and binned to depth intervals, *Lu* values were then used to calculate upward irradiance, E_u, as follows:

$$E_u\left(0^+,\ \lambda\right) = 4.5\ \cdot\ L_u(0^-,\ \lambda)\cdot\left(1-\rho(\lambda,\theta)/n_w^2(\lambda)\right) \tag{6}$$

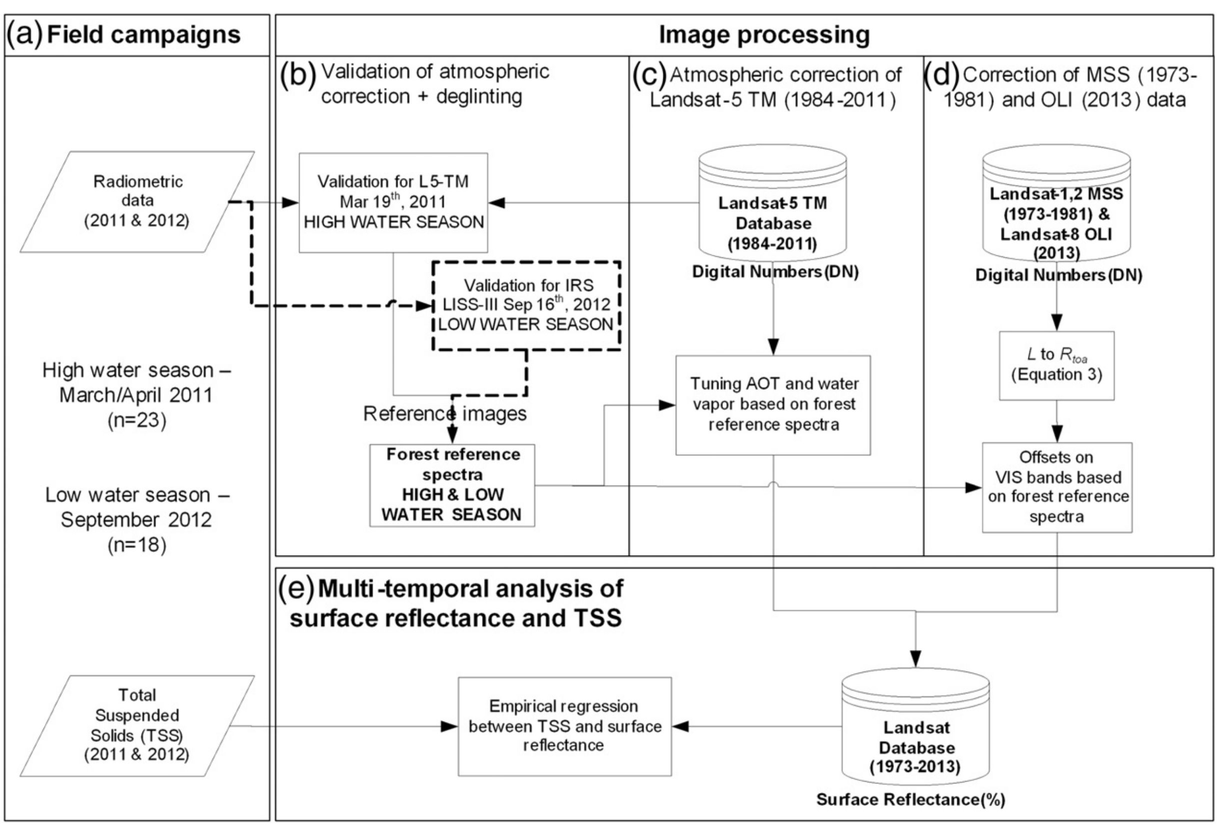

Fig. 2. Flow-chart of the methodology applied in this study. Field data of two campaigns (a) was used to calibrate the atmospheric correction (b) that was applied to Landsat-5 TM database based on forest reference spectra (c). After incorporating corrected MSS and OLI surface reflectance into the database (d), a multi-temporal analysis of $\rho_{surf}(\lambda)$ and of TSS in four sub-basins and along the Tapajós River was performed (e).

where $\rho(\lambda, \theta)$ is Fresnel reflectance index of the water (0.021) and $n_w^2(\lambda)$ is Fresnel refractive index (1.34) which relates to the fraction of the incident irradiance of a collimated beam that is reflected by a level surface (Mobley, 1994). Next, surface reflectance, $\rho_{surf}(\lambda)$, values were calculated for each profile according to:

$$\rho_{surf}(\lambda) = E_u\left(0^+, \lambda\right) / E_s\left(0^+, \lambda\right). \tag{7}$$

4.2. Image processing

The image processing for atmospheric correction and normalization of all selected Landsat data (1973–2013) from DN to ρ_{surf} was performed in four steps: i) imagery selection and compilation into a database; ii) atmospheric correction of two image sets (from high water level and low water level seasons—called reference images) coincident with *in situ* radiometric measurements; iii) correction of atmospheric effects from all Landsat-5 TM images (1984–2011) using the references images and AERONET data to optimize the 6S input atmospheric parameters for each image; iv) correction of MSS and OLI data from DN to ρ_{TOA} followed by normalization to ρ_{surf} based on forest spectra derived from reference images.

4.2.1. Imagery database

The detectable water bodies in the Tapajós River Basin extend over six Landsat TM scenes (Fig. 1). Landsat MSS and TM images acquired from 1973 to 2011 were downloaded from DGI/INPE (2013) for analysis of two specific seasons: high water level season (March to May) and low water level season (August to November). Recent cloud free images from the OLI sensor, on board Landsat-8, acquired in April and September 2013, were downloaded from EarthExplorer website (USGS, 2013a). A total of 77 images (31 from high season and 46 from low season) were incorporated into the database (Table 1).

4.2.2. Atmospheric correction validation

In order to define images that can be used as references to correct historical Landsat data, two groups of satellite images corresponding to the field work periods were corrected for atmospheric effects, and validated with *in situ* radiometric data. The statistical parameters used for evaluation were the determination coefficient (R^2), regression slopes, and the RMSE (root mean square error). After atmospheric correction, glint effect was removed according to Eq. (6) and their statistical parameters were also compared.

Table 1
Number of satellite images of six orbit/rows acquired in high and low water seasons between 1973 and 2013 used in the image processing. Note that only months that represent at least one image are shown.

		High water level			Low water level			
		Mar	Apr	May	Aug	Sep	Oct	Nov
MSS	1973				4			
	1975				2			
	1979				2	1		
	1980				1	1		
	1981			3				
TM	1984		1	1	1	2		1
	1985			2			1	
	1986			1				
	1987		1	1			1	1
	1989				2	2		
	1990	1	1					
	1993			5	1	4		
	1995				1			
	1996		1					
	1997			3	2		1	
	1998				1			
	1999			1				
	2000				3			
	2001		1	1				
	2005		1	1		2	2	
	2011	3			1		1	
OLI	2013		2			5		

For the field work performed in March/April 2011 during the high water level season, three Landsat-5 TM images (row/orbit: 227/63; 228/63; and 228/64) acquired on March 19, 2011 were used in the validation process. However, for the campaign performed in September 2012, Landsat-5 was no longer active, which prevented full seasonal analysis of Landsat data. Alternatively, cloud-free images acquired by IRS LISS-III in the same period of the campaign were used as reference images for the low water level season.

The input data for the 6S model were provided by iteratively testing measured ranges of water vapor values and AOT from the closest AERONET (AErosol RObotic NETwork) station (NASA/GSFC, 2013), near Belterra (S 3°06′, W 55°03′, see Fig. 1). Data available from 1999 to 2005 shows water vapor values of 4.2 ± 0.6 cm, and AOT of 550 nm varying from 0.1 up to 0.5 (dimensionless). For Landsat-5 TM (March 19, 2011), a water vapor value of 3.8 cm and AOT equal to 0.22 were chosen, minimizing the average difference between *in situ* and image reflectance output. Using the same criteria, LISS images (September 16, 2012) were atmospherically corrected by a physical-based method having water vapor value and AOT equal to 3.7 cm and 0.19, respectively.

4.2.3. Atmospheric correction of historical Landsat-5 TM data (1984–2011)

Once the atmospheric corrections of the reference images were validated, they were used to iteratively define the set of input values for running the atmospheric correction on the 6S model. The set of water vapor values and AOT for each TM image were defined by minimizing the differences between forest spectra from the reference images and the image subjected to atmospheric correction.

The assumption is that densely forested areas present invariant spectra over decades that can be used as reference spectra to optimize atmospheric correction in individual scenes (Holben et al., 1998; Kaufman et al., 1997; Liew et al., 2009). Although Amazonian forest spectra is very steady over decades, there are slight differences between spectra taken in rainy and dry seasons (Asner, 1998; Lu, Mausel, Brondízio, & Moran, 2004; Lu et al., 2002) that must be taken into account for proper imagery correction. As such, the images acquired during the high water level season (or rainy season) were optimized to forest spectra from Landsat 5-TM acquired in March 19, 2011, while images acquired during the low water level season (or dry season) were optimized using LISS-III acquired in September 2012 as reference. After optimizing the atmospheric parameters (water vapor and visibility) for each TM image, vegetation spectra were extracted and averaged differences compared with the reference images. Images that did not fall within an acceptable range (up to 50% difference at red band, which corresponds to a difference of up to 1.5% in ρ_{surf} and have minimum impact on TSS estimation) were re-corrected with new atmospheric parameters.

4.2.4. Correction of MSS and OLI data

The 6S physical-based model does not have the functionality to correct MSS and OLI imagery; as such, an alternative procedure had to be adopted for atmospheric correction of these images. MSS images were first converted from DN to $L(\lambda)$ (Markham & Barker, 1986), and subsequently corrected to $\rho_{TOA}(\lambda)$ (see Eq. (3)) according to the radiometric specifications and the date of image acquisition. OLI DN data were converted to $\rho_{TOA}(\lambda)$ according to USGS's website (USGS, 2013b). For both MSS and OLI $\rho_{TOA}(\lambda)$, the atmospheric effects were removed from VIS bands by applying an offset to match dense forest spectra with those from optimized surface reflectance (see Fig. 4a) which resulted in $\rho_{surf}(\lambda)$. In this case, we assumed that the differences between the surface reflectance forest spectra extracted from reference images and the forest $\rho_{TOA}(\lambda)$ from MSS and OLI data can be attributed to atmospheric effects.

4.3. Multi-temporal analysis of surface reflectance and TSS concentration

Once surface reflectance at visible and NIR were derived from the imagery database (Landsat-MSS, Landsat-TM, and OLI), a temporal analysis was performed in four different sub-basins and along the Tapajós River (see Fig. 1), for a total of eight different sites. The sites were chosen in order to cover the four main tributaries in terms of water discharge and mining activities (Crepori, Jamanxim, Tocantins, and Novo rivers) and also four other sites along the Tapajós River that represent the river's longitudinal variation from upstream to the mouth (Jacareacanga, Itaituba, Aveiro, and Santarém). For each site, several pixels distributed in the sample area were selected and averaged to reduce the variability caused by adjacency or bottom effects, and also to diminish the natural variability of the water body. This procedure can also minimize the different spatial resolution of MSS (80 m) and TM (30 m) data. Furthermore, in order to avoid adjacency effect on the selected pixels, the analyses were restricted to rivers with at least 3 pixels width. For that reason, MSS data could not be extracted at rivers with widths up to 200 m (e.g., Jamanxim, Novo, and Tocantins rivers), for which analyses were restricted to TM and OLI data (1984–2013).

In order to retrieve TSS concentration from surface reflectance in the eight sample sites, a non-linear regression was established between TSS and $\rho_{surf}(red)$ derived from reference images (see Fig. 6). The application of $\rho_{surf}(red)$ to estimate TSS in coastal and inland water using empirical regressions has been extensively reported for MSS (Harrington et al., 1992; Mertes et al., 1993) and TM data (Dekker et al., 2002; Masek et al., 2006). Averaged TSS collected during the two field works (n = 39) were used to establish the empirical regression curve that allows retrieving TSS with associated error estimation (within 95% level of confidence).

5. Results

5.1. Validation of atmospheric and glint correction

The evaluation of the atmospheric and glint correction revealed that the satellite ρ_{surf} without glint correction was in close agreement with *in situ* ρ_{surf} values, especially on the red and green wavebands (Fig. 3). High R^2 (>0.78) and low RMSE (<1.80 in ρ_{surf} unit) were observed for both seasons where regression coefficient (slope) values were around 0.85 at these bands (Table 2 shows the statistical results for the linear regressions shown in Fig. 3). At the blue (Landsat TM only) and NIR bands, the statistics show relatively poor results, with generally higher ρ_{surf} for satellite compared with *in situ* measurements (Fig. 3a and b).

Fig. 3c and d show examples of *in situ* ρ_{surf} spectra under different TSS concentrations plotted with glint corrected satellite $\rho_{surf}(\lambda)$ for the two field campaigns. High accordance between satellite and *in situ* $\rho_{surf}(red)$ is observed. According to Table 2, the correction for glint effect significantly improved the statistical results. At the blue band, R^2 values increased from 0.44 (no glint correction) to 0.80 (with glint correction), and RMSE decreased from 1.34 to 0.75 (in ρ_{surf} unit). Improvements were also observed for the green and red bands, where R^2 were higher than 0.88 and RMSE were lower than 1.0 (in ρ_{surf} unit) for both seasons. Because the images acquired in March 2011 (Landsat-5 TM) present high cloud coverage distributed unevenly over the scene, the SWIR signal can be attributed not only to glint effect, but also to atmospheric effects that have not been removed by the 6S model, and therefore minimizes the heterogeneity distribution of atmospheric conditions (Ruddick, Ovidio, & Rijkeboer, 2000). For LISS-III images, the $\rho_{surf}(SWIR)$ values were always lower than 1.0 (in ρ_{surf} unit), indicating that glint was not affecting the image quality. The statistical results corroborated this, however we followed the imagery analysis with the glint corrected LISS-III image given that the observed intercept values decreased when compared with no glint correction. All the linear regressions of deglinting data (shown in Fig. 3) were tested for normal distribution

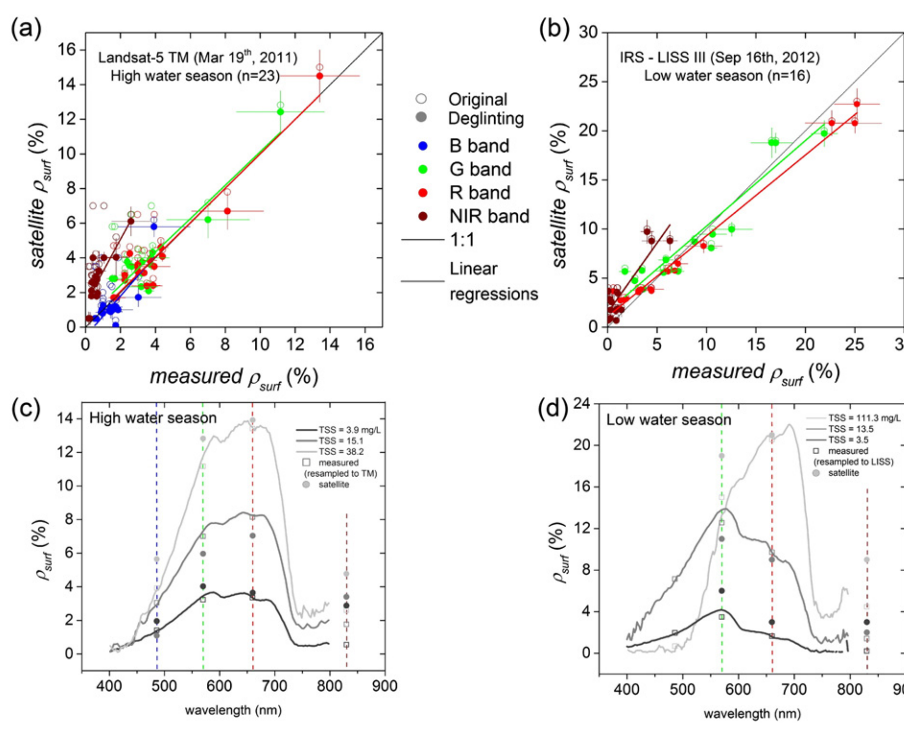

Fig. 3. Scatter plots between measured ρ_{surf} and corrected satellite ρ_{surf} at VNIR channels for (a) Landsat-5 TM, (b) IRS-LISS III. ρ_{surf} before (empty circles) and after (filled circles) glint removing is also shown. Linear regression and standard deviation are plotted only for deglinted data (best results). See Table 2 for statistical parameters of linear regressions. Note the different ρ_{surf} range between (a) and (b). Examples of measured surface reflectance spectra plotted with correspondent glint corrected satellite data for high water level (c) and low water level (d) seasons.

Table 2
Statistical parameters (intercept, slope, R^2, RMSE) for linear regressions before and after deglinting between measured $\rho_{surf}(\lambda)$ and $\rho_{surf}(\lambda)$ derived from two imagery sets: Landsat-5 (high water level) and LISS (low water level).

Channel		Landsat-5 TM (Mar. 19, 2011) – High water level (n = 23)				IRS LISS-III (Sep. 16, 2012) – Low water level (n = 16)			
		Intercept	Slope	R^2	RMSE	Intercept	Slope	R^2	RMSE
Blue		1.26	0.76	0.44*	1.34	–	–	–	–
	deglint	−0.51	1.16	0.80	0.75				
Green		2.1	0.82	0.78	1.56	1.57	0.87	0.88	1.77
	deglint	0.5	0.96	0.93	0.85	1.31	0.87	0.88	1.79
Red		1.7	0.88	0.88	1.36	1.35	0.82	0.97	0.89
	deglint	0.8	0.99	0.93	0.87	1.06	0.82	0.97	0.89
NIR		2.8	1.4	0.27*	1.36	1.77	1.41	0.75	1.46
	deglint	1.38	1.84	0.82	0.79	1.47	1.41	0.76	1.42

*Determination coefficients not significant at 0.05 level.

of residuals at a 0.05 level of significance. The results confirm that high and low water level data were drawn from a normally distributed population (tests not shown), thus indicating no over or under estimation of reflectance values.

5.2. Atmospheric correction of historical Landsat-5 TM data (1984–2011)

Once the atmospheric correction for the reference images was validated with *in situ* data, the forest spectra extracted from these images (Fig. 4a) were used as a reference to optimize the 6S atmospheric inputs (AOT, water vapor) for correction of the other 76 historical Landsat-5 TM images (Table 1). For this step, the imagery database was separated into two groups according to the time of imagery acquisition: high and low water level season. The rational for this division was the observed slightly higher forest spectra values at low water level (LISS-III) compared to forest spectra at high water level season (Landsat-5 TM). For example, $\rho_{surf}(green)$ reached values as high as 5.2% in the low water level, whereas for the images acquired during high water level season, values of 3.1% were observed (Fig. 4a).

The forest ρ_{surf} extracted from the historical images (Fig. 4b) was compared with the forest spectra from the reference images, again divided into low and high water level seasons (Tables 3 and 4). High accordance between forest spectra extracted from the corrected images and the reference images for both low (n = 30) and high water levels = (n = 28) periods was achieved. The highest differences between reference and individual images were observed at the blue band, where the average difference was about 33%. For the remaining bands, the differences were on average 9% for both low and high water level seasons.

5.3. MSS and OLI imagery correction

In total, 14 MSS and 7 OLI $\rho_{surf}(\lambda)$ images were incorporated into the database by applying offsets on uncorrected $\rho_{TOA}(\lambda)$ based on forest spectra. Because the atmospheric scattering effects are more prominent in the blue wavebands, the correction offset were consistently higher for blue band when compared to green and red bands. Fig. 4a depicts MSS and OLI $\rho_{TOA}(\lambda)$ corrected to $\rho_{surf}(\lambda)$. For example, MSS and OLI $\rho_{TOA}(green)$ were corrected from 8.1 and 6.2%, respectively, to $\rho_{surf}(green)$ of 4.6%.

5.4. Spatial and temporal analysis of surface reflectance

Once the correction for imagery database (Landsat MSS, TM, and OLI) was validated, a multi-temporal analysis of $\rho_{surf}(\lambda)$, from 1973 to 2013, was performed for four tributaries (Jamanxim, Tocantins, Crepori, and Novo rivers) and along the Tapajós River (see Fig. 1). Given the coarse spatial resolution of the MSS data (80 m), the Jamanxim, Tocantins, and Novo rivers were not sampled due to signal interferences

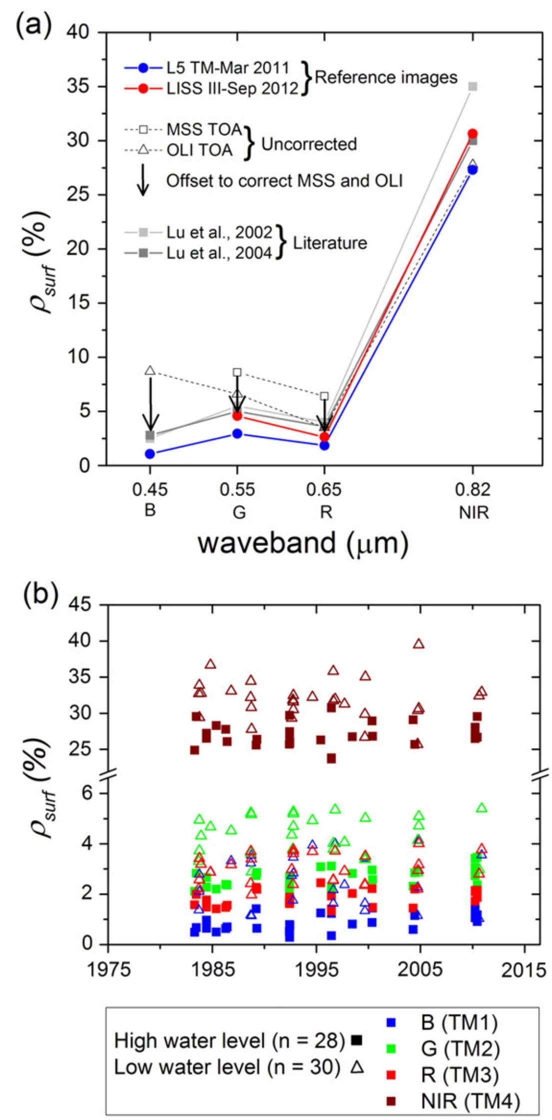

Fig. 4. (a) Dark dense forest spectra extracted from high water level season (Landsat) and low water season (LISS-III) used as reference for optimizing atmospheric parameters on Landsat historical data. Examples of uncorrected MSS and OLI TOA reflectance, and dense forest from the Brazilian Amazon found in literature (Lu et al., 2002, 2004) are also shown. (b) Dense forest spectra for high and low water seasons extracted from historical Landsat-5 TM images having spectra shown in (a) as reference. See Tables 3 and 4 for differences between reference images and historical TM data.

from surrounding vegetation on the water reflectance from the narrow rivers. Therefore, for these rivers, time series analysis of $\rho_{surf}(\lambda)$ starts in 1984 with TM data.

In general, besides the signal differences among rivers, two major temporal variations of water $\rho_{surf}(\lambda)$were observed: seasonal, between low and high water level season, and annual (Fig. 5). Although differences in magnitude among the rivers were observed, $\rho_{surf}(VNIR)$ values from the low water season were consistently higher than those from the high water season, especially at red and green bands. In terms of inter-annual analysis, a clear peak of ρ_{surf} in all bands was observed between 1985 and 1995 for the eight sites analyzed, with the least effect on Jacareacanga, located upstream of Tapajós River before the confluence with the heavily mined Crepori River.

For the Jamanxim River, located in a sub-basin with low mining activity, the $\rho_{surf}(red)$ values were lower than 4.0% in both seasons, but a significant difference ($p < 0.05$) was observed between high (1.7%) and low (3.0%) water level seasons from 1984 to 2013 (Fig. 8). At the other extreme, in the Crepori sub-basin, characterized by intense

Table 3
Differences between dense forest spectra ($\rho_{surf}(\lambda)$), extracted from high water level season reference images (L5 TM March 2011) and historical images acquired at the same season. SD – standard deviation.

					Blue	Green	Red	NIR
Reference image (Landsat 5 Mar 2011) ρ_{surf}± SD					1.2 ± 0.2	3.1 ± 0.3	2.0 ± 0.3	27.3 ± 2.3
	Orbit	Row	Date	Season	Percentage difference from reference image $(x_m - x_i/x_m).100$			
L5-TM	229	64	04/06/1984	High	59%	9%	0%	−8%
L5-TM	228	64	30/05/1985	High	27%	28%	27%	0%
L5-TM	227	64	10/05/1986	High	79%	31%	31%	−4%
L5-TM	229	64	09/04/1987	High	63%	25%	28%	−2%
L5-TM	228	64	09/03/1990	High	−24%	12%	−14%	6%
L5-TM	229	64	11/05/1993	High	77%	30%	17%	6%
L5-TM	229	64	19/05/1996	High	−6%	−1%	−25%	4%
L5-TM	228	64	31/05/1997	High	−4%	−2%	3%	−13%
L5-TM	227	64	30/05/1999	High	44%	9%	−2%	2%
L5-TM	228	64	10/05/2001	High	−27%	18%	28%	2%
L5-TM	228	64	03/04/2005	High	68%	27%	29%	−6%
Historical average ρ_{surf}± SD					1.0 ± 0.4	2.8 ± 0.5	1.9 ± 0.4	27.2 ± 1.8

mining activity, the $\rho_{surf}(red)$ values increased from 4.0% in 1973 to 27.0% in 1984, reaching its maximum value in 1993 (36.0%), during low water level season. Although values decreased in the following decades, their magnitudes were still high (up to 20%) until 2013. The Tocantins and Novo rivers presented similar results, the highest of $\rho_{surf}(green)$ and $\rho_{surf}(red)$ in the early 1990s. However, for the Tocantins and Novo rivers, a recent (2005–2013) increase of reflectance was observed for the same bands, indicating that considerable mining activity is currently taking place in these sub-basins.

The analysis of $\rho_{surf}(\lambda)$ along the Tapajós River (Jacareacanga, Itaituba, Aveiro, and Santarém) showed values not higher than 5% from the upstream (Jacareacanga) to the mouth (Santarém) at the high water period for the entire time series (1973–2013). During the low water period, however, significantly ($p < 0.05$) higher values ($\rho_{surf}(green) = 5\%$ on average) were observed compared to the high water level season (3% on average). Although low $\rho_{surf}(\lambda)$ were observed upstream (Jacareacanga) at green and red bands, a considerable increase of reflectance was observed in Itaituba and, less pronounced, in Aveiro (which is 200 km downstream from Itaituba), mainly in the period between 1985 and 1995. Taking into account the river's network and discharge, the $\rho_{surf}(\lambda)$ variation from upstream Tapajós (Jacareacanga) observed for both seasons is in accordance with the spatial variation of the tributaries shown in Fig. 5a.

5.5. Spatial and temporal analysis of TSS

TSS concentrations were measured at 39 sample points and correlated with reflectance derived from satellite sensors (Landsat-5 TM data for high water level and LISS-III data for low water level season). Measured TSS concentrations were higher in those rivers with intense gold mining activity, such as the Crepori River. During high water level, TSS values of 35.3 mg/l were observed in this river, whereas in the low water period, concentrations up to 115.2 mg/l were measured. Minimum values are similar for both periods (Table 5).

The best empirical correlation between TSS and $\rho_{surf}(\lambda)$ was given by a power function ($R^2 = 0.94$, RMSE = 1.33%, see Fig. 6) using the red band. Although the curve is based on satellite $\rho_{surf}(red)$ up to 22%, we assumed that this function can be extended to values up to 35%, which corresponds to approximately 300 mg/l of TSS. It is worth noting the very similar correlation of TSS with *in situ* $\rho_{surf}(red)$ depicted by the dashed curve in Fig. 6. The TSS range available during fieldwork was only up to 110 mg/l, which corresponds to approximately 24% of satellite surface reflectance data. Above 35%, the empirical regression curve does not provide reliable TSS estimation because the regression's confidence range (confidence level = 95%) yields errors up to 50% (see confidence interval in Fig. 6).

Table 4
Differences between dense forest spectra ($\rho_{surf}(\lambda)$), extracted from low water level season master images (LISS-III September 2012) and historical images acquired at the same season. LISS-III sensor does not have a blue band. SD, standard deviation.

					Blue	Green	Red	NIR
Reference image (LISS-III Sept. 2012) ρ_{surf}± SD					–	4.6 ± 0.3	3.1 ± 0.2	30.6 ± 1.8
	Orbit	Row	Date	Season	Percentage difference from reference image $(x_m - x_i/x_m)\cdot 100$			
L5-TM	228	64	16/09/1984	Low	–	−8%	−9%	−11%
L5-TM	227	64	14/10/1985	Low	–	−2%	8%	−20%
L5-TM	228	62	11/10/1987	Low	–	1%	−1%	−8%
L5-TM	229	64	21/09/1989	Low	–	37%	37%	9%
L5-TM	229	64	16/09/1993	Low	–	17%	24%	−4%
L5-TM	229	64	05/08/1995	Low	–	−8%	−18%	−5%
L5-TM	228	64	03/08/1997	Low	–	12%	18%	−4%
L5-TM	227	64	31/08/1998	Low	–	11%	7%	−2%
L5-TM	229	64	18/08/2000	Low	–	26%	25%	3%
L5-TM	229	64	19/10/2005	Low	–	−11%	−28%	0%
L5-TM	229	64	01/08/2011	Low	–	35%	11%	−6%
Historical average ρ_{surf}± SD					2.6 ± 0.9	4.3 ± 0.7	3.0 ± 0.6	31.9 ± 2.7

Based on the defined power-law function (equation in Fig. 6), TSS values from the historical Landsat imagery at the eight sites analyzed were retrieved (Fig. 7). Following similar observed $\rho_{surf}(red)$ dynamic (Fig. 4), TSS exhibited higher concentrations at low water level than at high water level periods (Fig. 7). In the low water level season of 1989, for example, TSS values of about 301.0 mg/l were estimated for the Crepori River. After the Crepori discharge into the Tapajós River, the high TSS is mixed with the relatively low TSS waters of the Tapajós, and at approximately 260 km downstream, the TSS concentration decreased to about 33.5 mg/l at Itaituba City and down to 6.6 mg/l at the Santarém area. Similar values were observed for the high water season, but at lower TSS concentrations (Fig. 7); the Crepori River exhibited TSS values up to 100.0 mg/l, and after the confluence with the Tapajós River, TSS values decreased to 4.4 mg/l in Itaituba and to 2.5 mg/l in Santarém.

The spatial and seasonal dynamic is illustrated in Fig. 8, which corresponds to the seasonal $\rho_{surf}(red)$-based TSS variation (equation in Fig. 6) in the Crepori River and Tapajós River, from Landsat-8 images acquired on June 12th (high water) and September 16th (low water) 2013. An evident increase of TSS concentrations was observed from June 2013 (TSS = 38.0 mg/l) to September 2013 (96.0 mg/l). It is worth noting that the sediment plume in September reaches 100 km downstream in the Tapajós River after the confluence with the Crepori River, at a concentration of approximately 45.0 mg/l, decreasing to about 15.0 mg/l at the river's confluence (indicated in the Fig. 8).

6. Discussion

6.1. Atmospheric issues

Atmospheric correction is a key component prior to the analysis of satellite imagery time-series. However, difficulty rises due to the lack of information about past atmospheric conditions at the time of imagery acquisition, especially for remote areas such as the Amazon. In order to overcome the absence of information about atmospheric conditions required as input to physical-based atmospheric models, we applied an approach that relies on initial validation of a set of 6S atmospheric-corrected satellite images acquired concurrently to *in situ* reflectance data.

The *in situ* reflectance presented comparable values to those reported in literature for Amazonian waters (Barbosa, Novo, Melack, Gastil-Buhl, & Filho, 2010; Lobo, Novo, Barbosa, & Galvão, 2012; Rudorff, Galvão, & Novo, 2009) where *in situ* spectra data used for validation of the satellite images presented high variability at high magnitude values (see Fig. 3). This is likely due to signal-to-noise ratio reduction related to measuring under-water radiance in high TSS conditions (Reinart, Paavel, Pierson, & Strombeck, 2004; Sun et al., 2009). In high turbidity Amazonian water conditions, the under-water light is intensively attenuated in the visible spectrum, reducing signal-to-noise ratio and increasing data variability. Costa et al. (2013), for instance, have shown that sediment-rich waters (TSS = 138.8 mg/l) present a diffuse attenuation coefficient ($K_{d\ (\mathrm{blue})}$) five times higher (15.3 m^{-1}) than in a clear water river (TSS = 4.1 mg/l; $K_{d\ (\mathrm{blue})} = 3.0\ m^{-1}$).

Despite the variability of *in situ* reflectance, high correlations between *in situ* and satellite ρ_{surf} at the green and red bands indicate that the atmospheric correction approach was successful. Green and red bands also correspond to the spectrum where suspended solids present a high scattering property, which increases the signal-to-noise ratio of the signal detected by remote sensors. On the other hand, for blue and NIR bands the atmospheric correction resulted in a general over estimation of ρ_{surf} when compared to *in situ* ρ_{surf}. The weak correlation between measured and satellite $\rho_{surf}(blue)$ suggests that the atmospheric method did not properly model the effects of aerosol and gases scattering (Guanter et al., 2010) and absorption effects by nitrogen dioxide (Gao, Montes, Davis, & Goetz, 2009; O'Neill & Costa, 2013). Studies that validated atmospheric correction with *in situ* radiometric measurements attributed the errors at blue wavelengths either to the inability of the physical-based approach to model aerosol and gases concentration (Bailey & Werdell, 2006; Ruddick et al., 2000), or to unavailability of a suitable aerosol model (Guanter et al., 2010). The effects will be more accentuated in moderate concentrations of absorbing aerosols as higher concentrations are often identified as clouds.

At the NIR region of the spectrum, the poor correlation between measured and corrected satellite $\rho_{surf}(NIR)$ is likely due to the low magnitude (up to 5%) and to the adjacency effect on the reflectance signal. The low magnitude and low variation of $\rho_{surf}(NIR)$ is mostly due to strong absorption of NIR radiation by water molecules (Mobley, 1994). Although considerable $\rho_{surf}(NIR)$ has been observed in turbid waters, as reported in literature (Dekker et al., 2001; Liew et al., 2009; Wang & Shi, 2007), the NIR spectrum from clear waters (TSS < 7.0 mg/l) should be close to zero. Given the small width of the tributaries in this study, the overestimated satellite $\rho_{surf}(NIR)$ in the clear waters can thus be attributed mostly to the adjacency effect. Santer and Schmechtig (2000) investigated the contribution of the adjacency effect to the NIR water reflectance in the middle of a circular lake. For a lake with 5 km radius, the supplementary contribution of the surrounding reflectance to the NIR water signal was roughly half of the water signal. The adjacency contribution can be even higher at lower distances, which is the case of the Tapajós River Basin, where some tributaries are no larger than 110 m in width (e.g., Tocantins and Novo rivers). The representation of the adjacency effect is minimal on VIS bands, because forest spectra present low ρ_{surf} (up to 5%) as opposed to NIR, where values are as high as 40%. As such, caution should be taken when using NIR bands to derive turbidity from narrow rivers, given the difficulty in defining the spatial contribution of the adjacency signal to the $\rho_{surf}(NIR)$ from water bodies.

The glint effect correction approach was successful, as shown by the improved correlations between measured and satellite reflectance for the whole spectral range. The improvement was more evident on Landsat-5 TM (March 2011), when considerable cloud cover was observed in these images. We suggest that, besides the influence of a possible glint signal, the SWIR band (used in the deglinting process) might also contain atmospheric signal that was not totally removed in the atmospheric correction approach. Because the 6S correction method considers AOT and water vapor to be homogenous in the entire scene, this deglinting procedure can correct non-homogenous atmospheric effects within a satellite image, and as such provides a more accurate estimate of water ρ_{surf} (Kutser, Vahtmäe, Paavel, & Kauer, 2013; Wang & Shi, 2007). This is particularly important to remote sensing studies in the Amazon, where high humidity and high cloud cover introduces atmospheric variability within the same scene (Lu et al., 2002).

6.2. Multi-temporal analysis of $\rho_{surf}(\lambda)$ and TSS in the Tapajós River Basin

The results of the corrections performed in historical Landsat imagery (1973–2013) demonstrated that forest spectra from historical Landsat-5 TM (1984–2011) behaved as an invariant spectral feature over decades, considering the seasonality. Therefore, any $\rho_{surf}(\lambda)$ variation in spectra extracted from water bodies can be attributed mostly to variation in optical constituents in the water and not to environmental conditions, such as atmospheric and glint effects. According to the validation procedure (Section 5.1), the certainty of corrected ρ_{surf} is higher for the red and green bands compared to the blue and NIR, where satellite ρ_{surf} are overvalued.

The magnitude and spectral shape of $\rho_{surf}(\lambda)$ derived in this study is similar to other studies in the Amazonian waters (Lobo et al., 2012; Rudorff et al., 2009). In general, increasing TSS concentration up to 50.0 mg/l affects primarily the green and red wavebands. Under very high turbidity conditions (TSS >100.0 mg/l), the light scattered by suspended particles also considerably affects the NIR spectrum region. For instance, spectra derived from sediment-rich waters in this study (TSS up to 110.0 mg/l) present values (up to 23.1% at red band) in accordance with other studies in the Amazon River floodplain (Barbosa et al., 2010; Mertes et al., 1993; Rudorff et al., 2009). The observed reflectance values are likely associated with the origin of the inorganic particles. TSS derived from mining activities in the Tapajós is composed mostly of silt/clay particles (Telmer & Stapper, 2007), which in turn are more efficient at scattering light than organic and sand particles (Gordon et al., 2009). A recent laboratory investigation on the scattering properties of two suspended particle sizes has shown that clay/silt particles are 40% more efficient in scattering light than medium-sized sand particles at 660 nm (Bowers & Binding, 2006; Lobo et al., 2014). As a result, a high $\rho_{surf}(red)$ is expected from clay-rich water than from sand-rich waters, for example.

The imagery-derived surface reflectance from the Tapajós River Basin suggests that its variability is mainly affected by the scattering properties of suspended solids that vary seasonally and are also increased due to mining activities. Another possible source of inorganic matter to the water is deforestation (Neill et al., 2011). However, we believe that the possible increase in TSS caused by deforestation is not at the same magnitude as the increase in TSS caused by mining activity. For example, the Jamanxim River, which is characterized by highly deforested areas but with low mining activity in the sub-basin area (see Fig. 1), presents low $\rho_{surf}(\lambda)$ that are similar to those from Tapajós upstream (Jacareacanga), even in the low water level season when mining activity can be more intense. We would like to highlight that the natural clear water condition facilitates the detection of sediment plume caused by gold mining. The same rationale is likely not valid for white water (muddy water) rivers, such as the Madeira River in the Amazon. Because the Madeira River is naturally very turbid as a consequence of its drainage in the Andes, detection of gold mining tailings into the river is likely a more difficult task when comparing to the Tapajós clear water system.

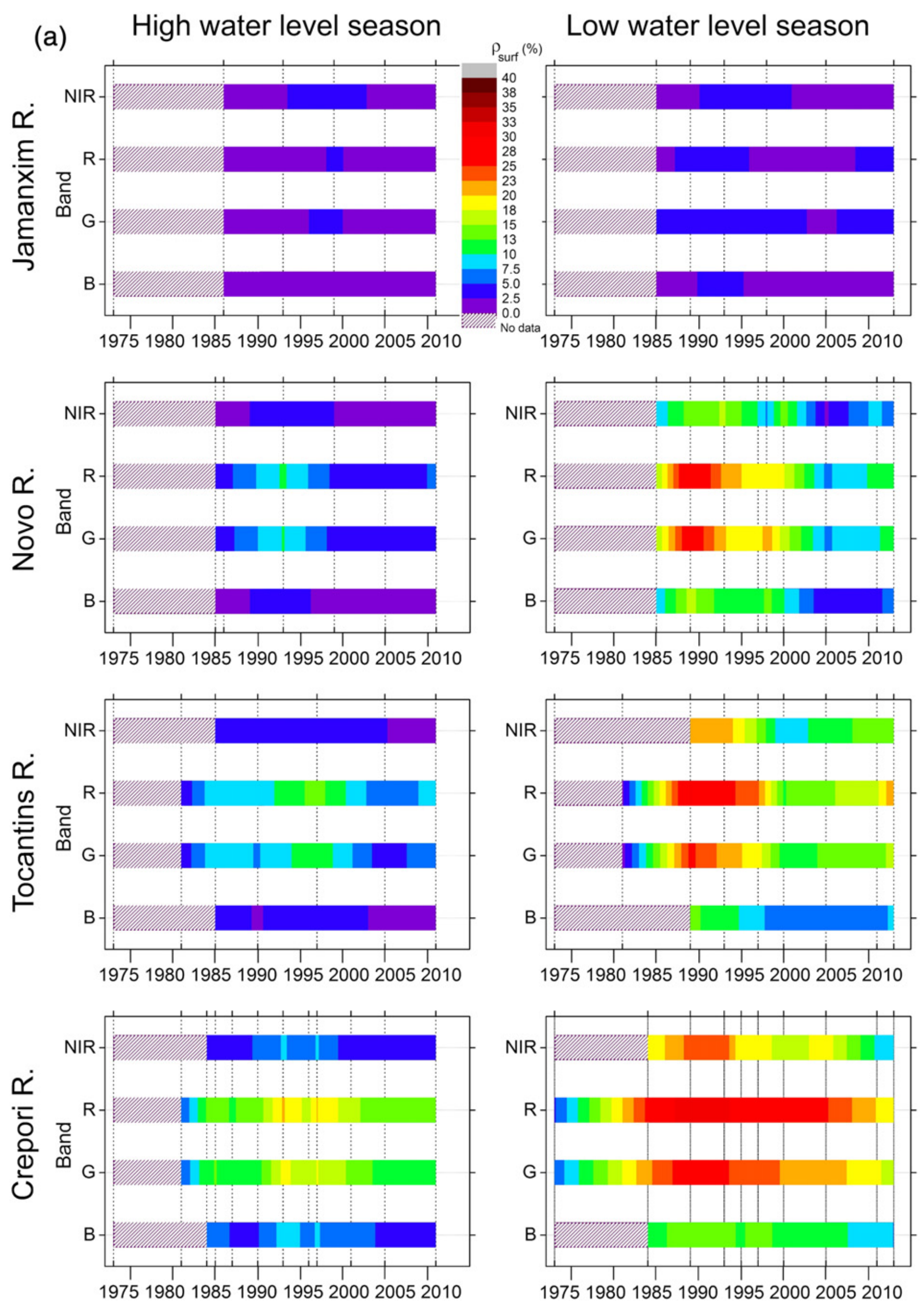

Fig. 5. Seasonal and inter-annual variation of $\rho_{surf}(VNIR)$ bands in four sub-basins: Jamanxim, Novo, Tocantins, and Crepori rivers; and along the Tapajós River: Jacareacanga, Itaituba, Aveiro, and Santarém cities used for location reference (see Fig. 1). The ρ_{surf} varies in the color palette from 0 (blue) up to 40%. The vertical dashed lines represent the available data used for plotting. Years with no data available are represented by the dashed bar.

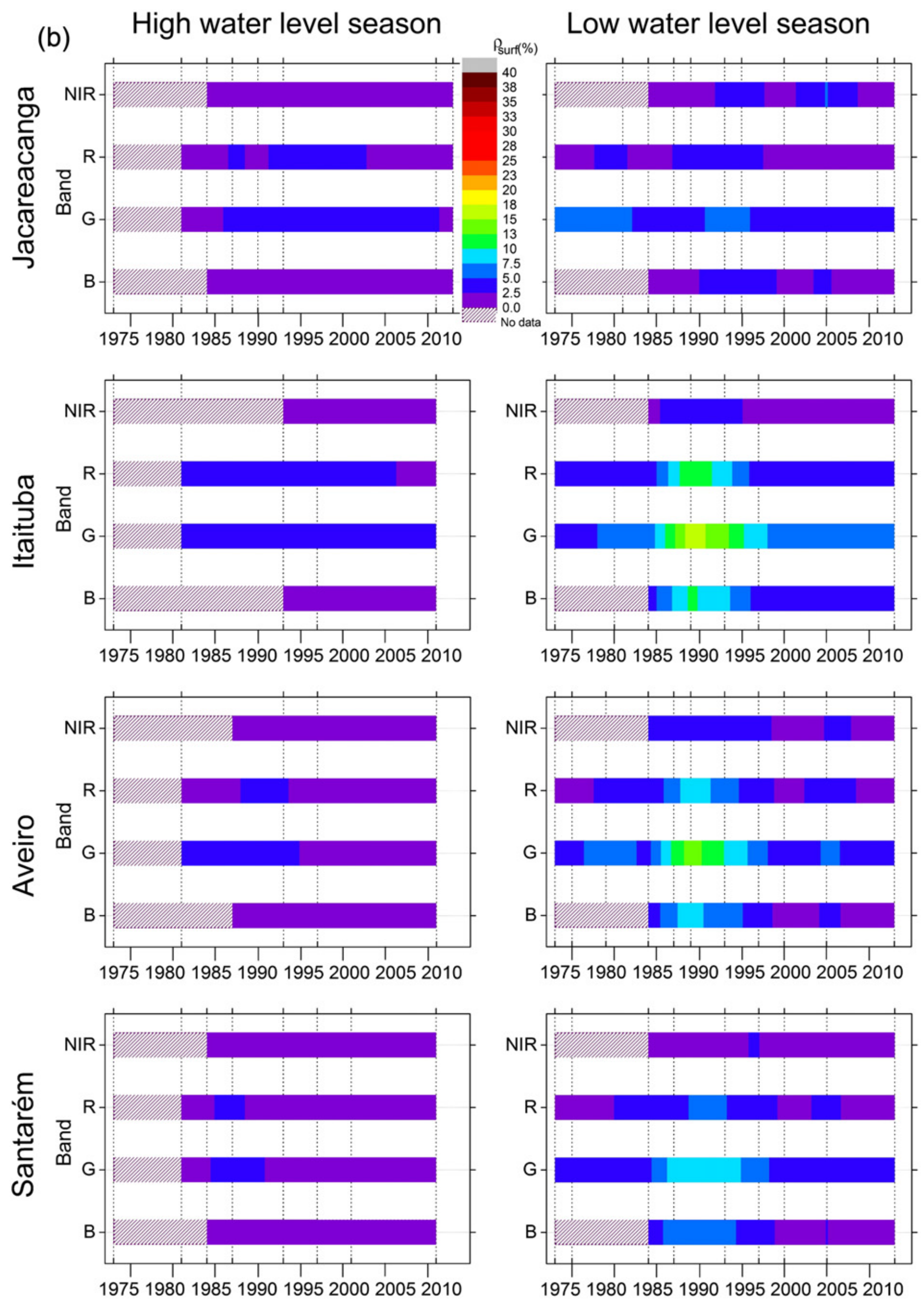

Fig. 5 (*continued*).

Seasonal variation of water quality and optical properties have been investigated in Amazonian water bodies (Barbosa et al., 2010; Casali et al., 2011; Costa et al., 2013; Kilham & Roberts, 2011; Novo et al., 2006). In general, differences between rising and ebbing periods in terms of TSS and light attenuation can be explained by factors such as hydrological regime flow, sediment transportation, and biogeochemistry of the water (Costa et al., 2013). In the Tapajós River Basin, the seasonal variation of TSS, and consequently, $\rho_{surf}(\lambda)$ can be explained by the synergism between hydrology, biogeochemistry dynamics, and gold mining activities. In terms of hydrological dynamic, Costa et al. (2013) reported that the increase of TSS in the Tapajós River (Santarém area) from ebbing (1.6 mg/l) to rising (4.1 mg/l) water periods can be explained by the suspended solids input carried during rain events, and also by sediment input from the floodplains as the waters rises.

Gold mining activities are also temporally dynamic. During the rainy season, most of the gold mining activity stops (Bezerra et al., 1998) and, associated with the increase in volume of water in the rivers, the sediment concentration dilutes. As a consequence, low reflectance caused by particle scattering is observed in this period. When the rainy season ends, the miners start working, and consequently high concentrations of sediment are observed in the rivers. This factor associated with low volume water results in TSS concentrations above 100 mg/l.

Besides seasonal variation, the results show a decadal change of TSS (Figs. 5 and 7). The highest TSS concentration is observed at the end of the 1980s and beginning of the 1990s for all sites, except for the

Jamanxim River where a quasi-constant decadal TSS is observed. During this period, the sediment plume derived from the Crepori, Novo, and Tocantinzinho rivers reached further downstream the Tapajós (Santarém site) where a TSS concentration above 6.0 mg/l was observed. The turbidity increment can be directly related to mining activity in the region. According to official estimates on gold production in the Tapajós region, the peak of gold production happened during this same period—end of the 1980s and beginning of the 1990s (Silva, 2012). Bezerra et al. (1998) reported that a total of 67 million m^3/year of sediment have been removed from the margins of many tributaries in the 1980s because of mining activities. In addition to sediment discharge from the tributaries, Telmer (personal communication, 2013) indicated that during that period, intense mining in the Tapajós River (Itaituba area) was performed by 'balsas' and pitch loaders, which are techniques that result in high TSS concentration in the water. Such activities were prohibited in the 1990s, which in turn directly reduced the TSS concentration (and $\rho_{surf}(red)$) in the following years, even with high TSS concentration discharges from Crepori River (see Fig. 5, Itaituba).

Another important factor that has triggered gold mining activity is the price of gold. In the 1980s, the price jumped from US$500 to US $2300/oz (adjusted for inflation, Fig. 9), thus encouraging artisanal gold miners to explore the area in more than 2000 mining sites. As a result, 30,000 people worked directly or indirectly with gold in this region during the 1980s (Bezerra et al., 1998). In the following years, the price of gold dropped and, to compensate, miners had to intensify gold production, increasing water siltation in the Crepori and Tocantins rivers (Fig. 9).

The price of gold stabilized during the 1990s, and in an association with surface gold exploitation, a decrease in mining activity was observed. Due to gold price increases in the last 3 years, a new gold rush is taking place (Silva, 2012). At this time, however, a more mechanical and industrial mining approach is extracting gold in deeper layers than artisanal gold mining can reach. Gold production in the 2010s is not as high as in the 1980s, but a significant increase in TSS concentration is observed (Tocantins and Novo rivers), suggesting that even mechanical and industrial mining discharges high amounts of sediment into the rivers.

7. Conclusions

The availability of relatively high spatial resolution multispectral satellite imagery since the 1970s is a unique resource to enhance our capability for understanding the spatial and temporal changes in inland water bodies caused by natural and anthropogenic forces. However, the use of time series satellite imagery to derive quantitative variables from the aquatic environment requires atmospheric correction and radiometric normalization of the imagery database. This study provides an analysis of a time series (1970s to present) of satellite imagery acquired with the Landsat satellites for the purpose of evaluating the spatial temporal changes in sediment load from artisanal gold mining activities in the Tapajós River Basin, Amazon. We present an image processing method based on available models that corrects atmospheric effects, and, based on empirical relationship, estimates TSS concentration from historical Landsat data including MSS (1973–1981), TM (1984–2011), and OLI (2013) data. This imagery analysis allowed some important conclusions and recommendations.

First, it was shown that the 6S model provide statistically satisfactory results when compared to measured $\rho_{surf}(\lambda)$ from water bodies. The input AOT and water vapor were optimized based on ranges provided by AERONET, which is shown to be a reliable source of atmospheric information for the Amazon. In addition, it was demonstrated that subtracting $\rho_{surf}(SWIR)$ from $\rho_{surf}(VNIR)$ improves correlations between *in situ* and satellite $\rho_{surf}(VNIR)$ by taking into account the effects of sunglint and possible heterogeneous distribution of aerosol and gases within the scene. Errors observed in the blue band are likely due to aerosol

Table 5
Descriptive statistics (average, standard deviation, minimum, and maximum values) of TSS concentration for the two field campaigns (high and low water level seasons).

	TSS (mg/l)	
	High water	Low water
Average	9.3	24.4
SD	10.1	42.7
Min	3.1	2.7
Max	35.3	115.2
n	23	16

scattering and gases (e.g. NO_2) absorption not fully simulated by the 6S model. Also, adjacency effects of surrounding vegetation can explain the overestimated satellite $\rho_{surf}(NIR)$. To minimize these effects, we suggest the use of models that take into account adjacency effects and allow better simulation of the gases effects.

For the atmospheric correction on historical Landsat imagery, we have shown that the use of dense forest spectra as reference to optimize atmospheric parameters for 6S is a sound alternative in areas with no information for atmospheric correction models. Similarly, by matching dense forest spectra as an alternative to the absence of 6S code, MSS and OLI surface reflectance imagery were incorporated in the analysis. This study demonstrates significant seasonality effects on forest spectra that must be taken into account for studies on temporal series in the Amazon, especially if using forest spectra as reference for image intercalibration or histogram matching.

Second, a robust empirical model between *in situ* TSS and concurrent satellite $\rho_{surf}(red)$ was established. The regression estimates TSS with high confidence from $\rho_{surf}(red)$ up to 25%. Above this value the uncertainty increases, suggesting further investigation on other methods to estimate TSS, such as bio-optical models. The combination of the atmospheric correction and the robust reflectance-based TSS model allowed the estimates of TSS independent of date of imagery acquisition.

Third, in regards to environmental changes, this study shows that the sediment load in the Tapajós River Basin is mostly derived from mining activities, which results in an increase of high light scattering TSS of a silt/clay nature. Further, a seasonal variation of water siltation is observed throughout the time frame of this study (1973–2013). During high water level, TSS concentrations are consistently lower than those from the low water period. The combination of high dilution and low mining activity explains lower TSS observed. Conversely,

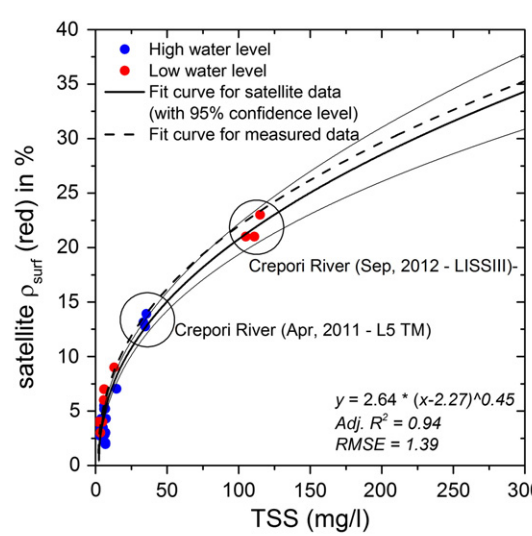

Fig. 6. Non-linear fit between TSS (n = 39) and reflectance (red band) derived from satellite sensors (TM data for high water level and LISS-III data for low water level season) including the 95% confidence range shown in solid thin lines. For comparison purposes, the fitting curve for measured reflectance is also plotted in the dashed line.

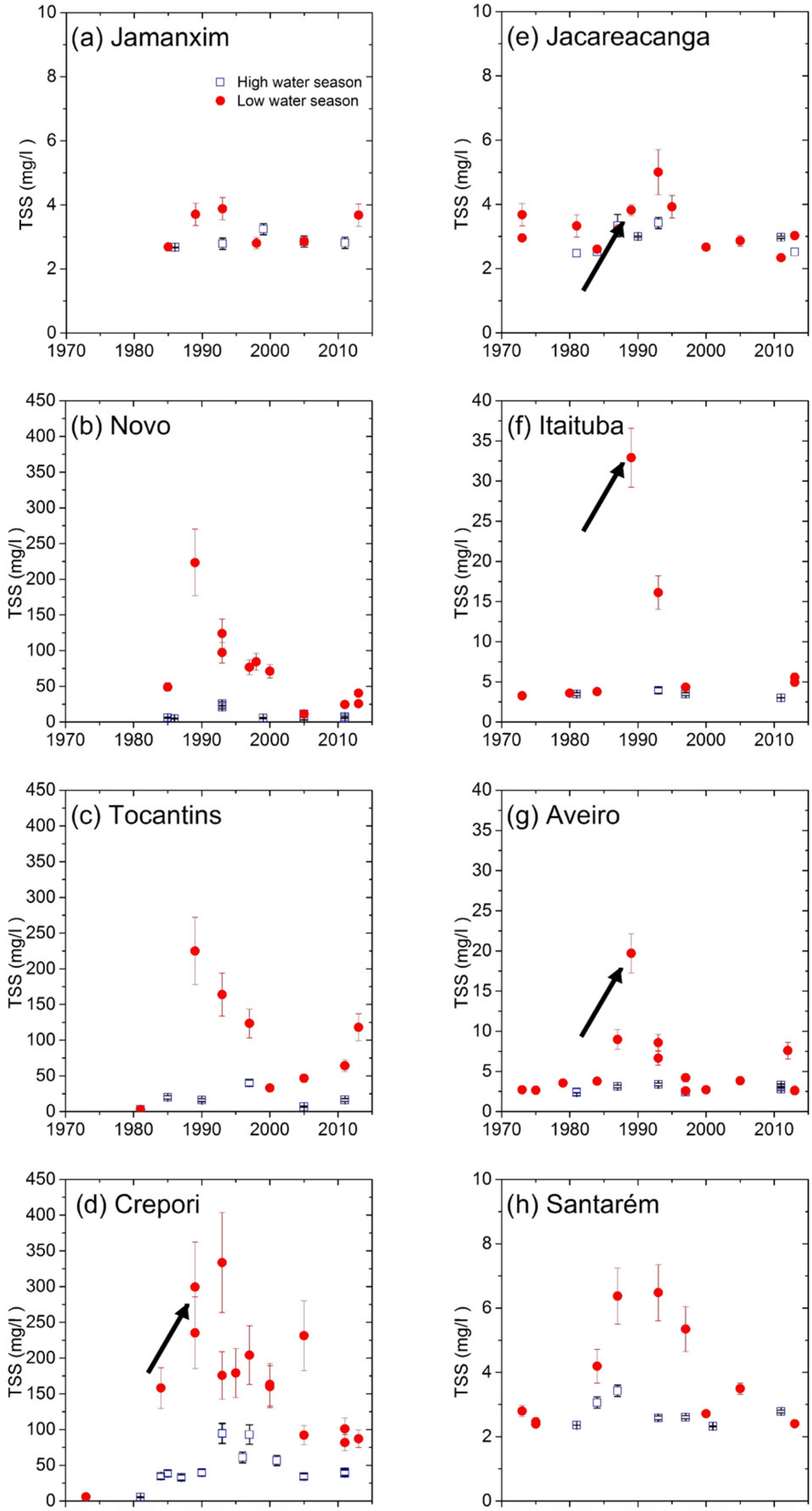

Fig. 7. TSS concentrations at eight locations retrieved from Landsat database (1973–2013) using the regression shown in Fig. 6. Examples given in the text are indicated by arrows. Note that the magnitude of the ordinate axis changes for the different rivers.

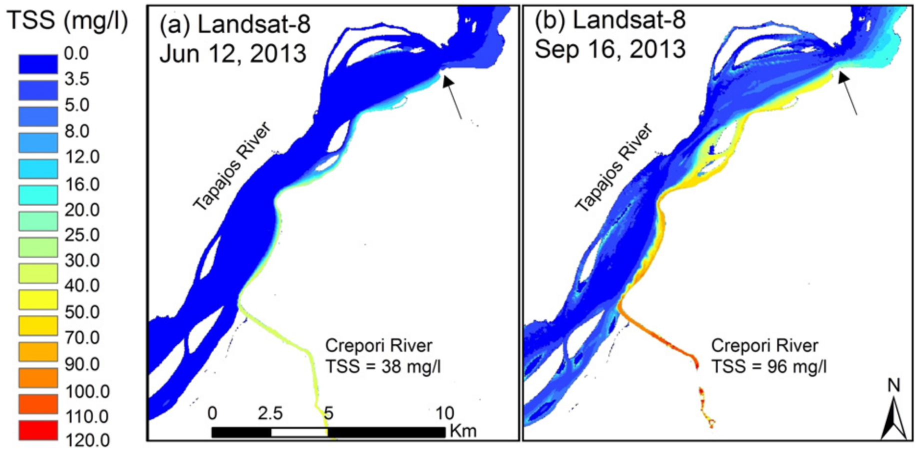

Fig. 8. TSS concentration at the Crepori River mouth into the Tapajós River retrieved from two Landsat-8 images: (a) June 12, 2013, high water level and (b) September 16, 2013, low water level period using the regression shown in Fig. 6. Arrows indicate the confluence in the river that mixes the water and TSS decreases.

during the low water level, the mining activity intensifies and combined with low volume of water, the TSS increases. In a decadal analysis, a peak of sediment concentration coincides with a peak of gold production in all sites analyzed motivated by high gold prices during the early 1990s. More recently, due to the current gold rush, a TSS increase has been observed mainly in the Novo and Tocantins rivers where industrial mining has been installed.

The $\rho_{surf}(VNIR)$ and TSS time series established in this paper provide valuable information about water quality changes over time and space in the Tapajós River Basin. Now, for this region, there is a quantified baseline of TSS, which represents the conditions in the 1970s before gold mining activities intensified to the current status. This article reports the seasonal and decadal variation of TSS in the most important tributaries, and indicates current hot spots of mining activity in the region. The product derived from this paper can support further investigation on how the sediment plume affects, for example, the depth/size of the euphotic zone available for primary production or further investigation on sediment transportation and precipitation process along the Tapajós River. Furthermore, as part of a multi-institute research project, the results will provide information for water quality monitoring and mining regulatory purposes. Lastly, the results show that current high-tech mining techniques cause similar water siltation impacts as artisanal gold mining. Therefore, it is important to adopt mining techniques that minimize the amount of TSS in the water if gold mining is to provide livelihoods for thousands of people in the Amazon.

Acknowledgments

This research was developed in a partnership between the University of Victoria (UVic) and the Brazilian Institute for Space Research (INPE). The authors would like to acknowledge logistical support by ICMBio (Brazilian Agency of Protected Areas) represented by MSc. Haroldo Marques. We also acknowledge financial support from the National Sciences and Engineering Research Council of Canada (NSERC) to Dr. Costa, FAPESP (Process 2011/23594-8) to Dr. Novo, and from *Brazilian Council for Scientific and Technological Development (CNPq)* (237930/2012-9), which supported the lead author as part of his PhD research project.

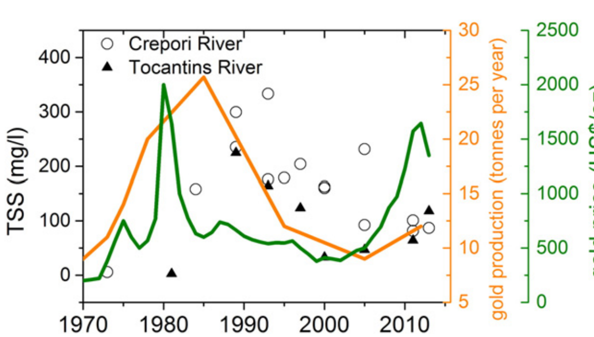

Fig. 9. Plot of the TSS concentration at the Crepori and Tocantins rivers, gold production in tonnes/year (Silva, 2012) in the Tapajós Area, and gold price (US$/oz) adjusted for inflation from 1970 to 2013. Source: DNPM (2013).

Appendix A. Supplementary data

Supplementary data associated with this article can be found in the online version, at http://dx.doi.org/10.1016/j.rse.2014.04.030. These data include Google maps of the most important areas described in this article.

References

Albert, A., & Mobley, C. D. (2003). An analytical model for subsurface irradiance and remote sensing reflectance in deep and shallow case-2 waters. *Optics Express*, *11*, 2873–2890.

ANA (2013). HidroWeb: Sistemas de informações hidrológicas. http://hidroweb.ana.gov.br (HidroWeb accessed in May, 2013)

APHA (2005). *Standard methods for the examination of water and wastewater.* Washington, D.C.: APHA-AWWA-WEF.

Araújo Neto, H. (2009). *Perfil do Ouro.* Brasília: Ministério de Minas e Energia.

Asner, G. P. (1998). Biophysical and biochemical sources of variability in canopy reflectance. *Remote Sensing of Environment*, *64*, 234–253.

Bailey, S. W., & Werdell, P. J. (2006). A multi-sensor approach for the on-orbit validation of ocean color satellite data products. *Remote Sensing of Environment*, *102*, 12–23.

Bale, A. J., Tocher, M.D., Weaver, R., Hudson, S. J., & Aiken, J. (1994). Laboratory measurements of the spectral properties of estuarine suspended particles. *Netherland Journal of Aquatic Ecology*, *28*, 237–244.

Barbosa, C., Novo, E., Melack, J., Gastil-Buhl, M., & Filho, W. (2010). Geospatial analysis of spatiotemporal patterns of pH, total suspended sediment and chlorophyll-a on the Amazon floodplain. *Limnology*, *11*, 155–166.

Bezerra, O., Veríssimo, A., & Uhl, C. (1998). *Impactos da garimpagem de ouro na Amazônia Oriental.* Belém/PA: Imazon.

Binding, C. E., Bowers, D.G., & Mitchelson-Jacob, E. G. (2005). Estimating suspended sediment concentrations from ocean colour measurements in moderately turbid waters; the impact of variable particle scattering properties. *Remote Sensing of Environment*, *94*, 373–383.

Bowers, D.G., & Binding, C. E. (2006). The optical properties of mineral suspended particles: A review and synthesis. *Estuarine, Coastal and Shelf Science*, *67*, 219–230.

Casali, S., Calijuri, M., Barbarisi, B., Renó, V., Affonso, A., Barbosa, C., et al. (2011). Impact of the 2009 extreme water level variation on phytoplankton community structure in Lower Amazon floodplain lakes. *Acta limnológica brasiliensia*, *23*, 260–270.

Costa, M. P. F., Novo, E. M. L. M., & Telmer, K. H. (2013). Spatial and temporal variability of light attenuation in large rivers of the Amazon. *Hydrobiologia*, *702*, 171–190.

CPRM (2009). Província mineral do Tapajós: Geologia, metalogenia e mapa previsional para ouro em SIG. http://www.cprm.gov.br (accessed in April, 2013)

Dekker, A. G., Vos, R. J., & Peters, S. W. M. (2001). Comparison of remote sensing data, model results and in situ data for total suspended matter (TSM) in the southern Frisian lakes. *Science of the Total Environment*, *268*, 197–214.

Dekker, A. G., Vos, R. J., & Peters, S. W. M. (2002). Analytical algorithms for lake water TSM estimation for retrospective analyses of TM and SPOT sensor data. *International Journal of Remote Sensing*, *23*, 15–35.

DGI/INPE (2013). Divisão de Geração de Imagens. www.dgi.inpe.br (accessed in May, 2013)

DNPM (2013). Sumário Mineral, 32. http://www.dnpm.gov.br/ (accessed in April, 2013)

Doxaran, D., Ehn, J., Bélanger, S., Matsuoka, A., Hooker, S., & Babin, M. (2012). Optical characterisation of suspended particles in the Mackenzie River plume (Canadian Arctic Ocean) and implications for ocean colour remote sensing. *Biogeosciences*, *9*, 3213–3229.

Gao, B. -C., Montes, M. J., Davis, C. O., & Goetz, A. F. H. (2009). Atmospheric correction algorithms for hyperspectral remote sensing data of land and ocean. *Remote Sensing of Environment*, *113*(Supplement 1), S17–S24.

Gong, S., Huang, J., Li, Y., & Wang, H. (2008). Comparison of atmospheric correction algorithms for TM image in inland waters. *International Journal of Remote Sensing*, *29*, 2199–2210.

Gordon, H. R., & Brown, O. B. (1975). Multiphase Monte-Carlo technique for simulation of radiative-transfer. *Journal of Quantitative Spectroscopy & Radiative Transfer*, *15*, 419–422.

Gordon, H. R., Lewis, M. R., McLean, S. D., Twardowski, M. S., Freeman, S. A., Voss, K. J., et al. (2009). Spectra of particulate backscattering in natural waters. *Optics Express*, *17*, 16192–16208.

Gordon, H. R., & Wang, M. (1994). Retrieval of water-leaving radiance and aerosol optical thickness over the oceans with SeaWiFS: A preliminary algorithm. *Applied Optics*, *33*, 443–452.

Guanter, L., Ruiz-Verdú, A., Odermatt, D., Giardino, C., Simis, S., Estellés, V., et al. (2010). Atmospheric correction of ENVISAT/MERIS data over inland waters: Validation for European lakes. *Remote Sensing of Environment*, *114*, 467–480.

Guenther, M., & Bozelli, R. (2004). Effects of inorganic turbidity on the phytoplankton of an Amazonian Lake impacted by bauxite tailings. *Hydrobiologia*, *511*, 151–159.

Hadjimitsis, D.G., & Clayton, C. (2009). Assessment of temporal variations of water quality in inland water bodies using atmospheric corrected satellite remotely sensed image data. *Environmental Monitoring and Assessment*, *159*, 281–292.

Harrington, J. A., Jr., Schiebe, F. R., & Nix, J. F. (1992). Remote sensing of Lake Chicot, Arkansas: Monitoring suspended sediments, turbidity, and Secchi depth with Landsat MSS data. *Remote Sensing of Environment*, *39*, 15–27.

Hedley, J.D., Harborne, A.R., & Mumby, P. J. (2005). Technical note: Simple and robust removal of sun glint for mapping shallow-water benthos. *International Journal of Remote Sensing*, *26*, 2107–2112.

Hochberg, E. J., Andrefouet, S., & Tyler, M. R. (2003). Sea surface correction of high spatial resolution Ikonos images to improve bottom mapping in near-shore environments. *IEEE Transactions on Geoscience and Remote Sensing*, *41*, 1724–1729.

Holben, B. N., Eck, T. F., Slutsker, I., Tanré, D., Buis, J. P., Setzer, A., et al. (1998). AERONET—A Federated Instrument Network and Data Archive for Aerosol Characterization. *Remote Sensing of Environment*, *66*, 1–16.

Hu, C., Muller-Karger, F. E., Andrefouet, S., & Carder, K. L. (2001). Atmospheric correction and cross-calibration of LANDSAT-7/ETM + imagery over aquatic environments: A multiplatform approach using SeaWiFS/MODIS. *Remote Sensing of Environment*, *78*, 99–107.

INPE (2011). PRODES Project. www.obt.inpe.br (prodes accessed in Jun, 2011)

Junk, W. (1997). general aspects of floodplain ecology with special reference to Amazonian floodplains. In W. Junk (Ed.), *The Central Amazon Floodplain* (pp. 3–20). Berlin Heidelberg: Springer.

Kaufman, Y. J., Wald, A. E., Remer, L. A., Bo-Cai, G., Rong-Rong, L., & Flynn, L. (1997). The MODIS 2.1-μm channel-correlation with visible reflectance for use in remote sensing of aerosol. *IEEE Transactions on Geoscience and Remote Sensing*, *35*, 1286–1298.

Kilham, N. E., & Roberts, D. (2011). Amazon River time series of surface sediment concentration from MODIS. *International Journal of Remote Sensing*, *32*, 2659–2679.

Kirk, J. T. O. (2011). *Light and photosynthesis in aquatic ecosystems*. Cambridge, Cambs, UK; New York: Cambridge University Press.

Kutser, T., Vahtmäe, E., Paavel, B., & Kauer, T. (2013). Removing glint effects from field radiometry data measured in optically complex coastal and inland waters. *Remote Sensing of Environment*, *133*, 85–89.

Le, C. F., Li, Y. M., Zha, Y., Sun, D., & Yin, B. (2009). Validation of a quasi-analytical algorithm for highly turbid eutrophic water of Meiliang Bay in Taihu Lake, China. *IEEE Transactions on Geoscience and Remote Sensing*, *47*, 2492–2500.

Liew, S.C., Saengtuksin, B., & Kwoh, L. K. (2009). Monitoring turbidity and suspended sediment concentration of coastal and inland waters using satellite data. *Geoscience and Remote Sensing Symposium, 2009 IEEE International, IGARSS 2009* (pp. II-837-II-839).

Lobo, F. L., Costa, M. P. F., Phillips, S., Young, E., & McCregor, C. (2014). Light backscattering in turbid freshwater: A laboratory investigation. *Journal of Applied Remote Sensing*, *8*(1), http://dx.doi.org/10.1117/1.JRS.8.083611.

Lobo, F. L., Novo, E. M. L. d. M., Barbosa, C. C. F., & Galvão, L. S. (2012). Reference spectra to classify Amazon water types. *International Journal of Remote Sensing*, *33*, 3422–3442.

Lu, D., Mausel, P., Brondizio, E., & Moran, E. (2002). Assessment of atmospheric correction methods for Landsat TM data applicable to Amazon basin LBA research. *International Journal of Remote Sensing*, *23*, 2651–2671.

Lu, D., Mausel, P., Brondízio, E., & Moran, E. (2004). Relationships between forest stand parameters and Landsat TM spectral responses in the Brazilian Amazon Basin. *Forest Ecology and Management*, *198*, 149–167.

Markham, B. L., & Barker, J. L. (1986). Landsat MSS and TM Post-Calibration Dynamic Ranges, Exoatmospheric Reflectances and At-Satellite Temperatures. *EOSAT Landsat Technical Notes, No. 1 August 1986* http://landsathandbook.gsfc.nasa.gov/pdfs/L5_cal_document.pdf.

Masek, J. G., Vermote, E. F., Saleous, N. E., Wolfe, R., Hall, F. G., Huemmrich, K. F., et al. (2006). A Landsat surface reflectance dataset for North America, 1990-2000. *IEEE Geoscience and Remote Sensing Letters*, *3*, 68–72.

Mertes, L. A. K., Smith, M.O., & Adams, J. B. (1993). Estimating suspended sediment concentrations in surface waters of the Amazon River wetlands from landsat images. *Remote Sensing of Environment*, *43*, 281–301.

Mobley, C. D. (1994). *Light and water: Radiative transfer in natural waters*. Academic Press.

Moran, M. S., Bryant, R., Thome, K., Ni, W., Nouvellon, Y., Gonzalez-Dugo, M. P., et al. (2001). A refined empirical line approach for reflectance factor retrieval from Landsat-5 TM and Landsat-7 ETM+. *Remote Sensing of Environment*, *78*, 71–82.

NASA/GSFC (2013). Aerosol Robotic Network (AERONET). http://aeronet.gsfc.nasa.gov (in Mar, 2013)

Neill, C., Chaves, J. E., Biggs, T., Deegan, L. A., Elsenbeer, H., Figueiredo, R. O., et al. (2011). Runoff sources and land cover change in the Amazon: An end-member mixing analysis from small watersheds. *Biogeochemistry*, *105*, 7–18.

Novo, E. M. L., Barbosa, C. C., Freitas, R. M., Shimabukuro, Y. E., Melack, J. M., & Filho, W. P. (2006). Seasonal changes in chlorophyll distributions in Amazon floodplain lakes derived from MODIS images. *Limnology*, *7*, 153–161.

O'Neill, J.D., & Costa, M. (2013). Mapping eelgrass (*Zostera marina*) in the Gulf Islands National Park Reserve of Canada using high spatial resolution satellite and airborne imagery. *Remote Sensing of Environment*, *133*, 152–167.

Puttonen, E., Suomalainen, J., Hakala, T., & Peltoniemi, J. (2009). Measurement of reflectance properties of asphalt surfaces and their usability as reference targets for aerial photos. *IEEE Geoscience and Remote Sensing*, *47*, 2330–2339.

Reinart, A., Paavel, B., Pierson, D., & Strombeck, N. (2004). Inherent and apparent optical properties of Lake Peipsi, Estonia. *Boreal Environment Research*, *9*, 429–445.

Rodrigues, R. M. (1994). *Estudo dos impactos ambientais decorrentes do extrativismo mineral e poluição mercurial no Tapajós—Pré-Diagnóstico*. Rio de Janeiro: CETEM/CNPq.

Roland, F., & Esteves, F. D. (1998). Effects of bauxite tailing on PAR attenuation in an Amazonian crystalline water lake. *Hydrobiologia*, *377*, 1–7.

Ruddick, K. G., Ovidio, F., & Rijkeboer, M. (2000). Atmospheric Correction of SeaWiFS Imagery for Turbid Coastal and Inland Waters. *Applied Optics*, *39*, 897–912.

Rudorff, C. M., Galvão, L. S., & Novo, E. M. L. M. (2009). Reflectance of floodplain waterbodies using EO-1 Hyperion data from high and receding flood periods of the Amazon River. *International Journal of Remote Sensing*, *30*, 2713–2720.

Santer, R., & Schmechtig, C. (2000). Adjacency effects on water surfaces: Primary scattering approximation and sensitivity study. *Applied Optics*, *39*, 361–375.

Schueler, V., Kuemmerle, T., & Schroeder, H. (2011). Impacts of surface gold mining on land use systems in Western Ghana. *Ambio*, *40*, 528–539.

Silva, A.R. (2012). *A indústria mineral no Pará*. (Belém, PA.).

Sousa, R. N., & Veiga, M. M. (2009). Using performance indicators to evaluate an environmental education program in artisanal gold mining communities in the Brazilian amazon. *Ambio*, *38*, 40–46.

Sun, D., Li, Y., Wang, Q., Le, C., Huang, C., & Wang, L. (2009). Parameterization of water component absorption in an inland eutrophic lake and its seasonal variability: A case study in Lake Taihu. *International Journal of Remote Sensing*, *30*, 3549–3571.

Telmer, K. (2013). Personnal communication. In. Victoria, B.C.

Telmer, K., Costa, M., Simões Angélica, R., Araujo, E. S., & Maurice, Y. (2006). The source and fate of sediment and mercury in the Tapajós River, Pará, Brazilian Amazon: Ground- and space-based evidence. *Journal of Environmental Management*, *81*, 101–113.

Telmer, K., & Stapper, D. (2007). Evaluating and monitoring small scale gold mining and mercury. *Building a Knowledge-base with Satellite Imagery and Field Work. UNIDO Project EG/GLO/01/G34, Final Report*. (pp. 1–49) (November).

Tudesque, L., Grenouillet, G., Gevrey, M., Khazraie, K., & Brosse, S. (2012). Influence of small-scale gold mining on French Guiana streams: Are diatom assemblages valid disturbance sensors? *Ecological Indicators*, *14*, 100–106.

USGS (2013a). Earth Explorer. http://earthexplorer.usgs.gov (accessed in Sep, 2013)

USGS (2013b). Using the USGS Landsat 8 Product. https://landsat.usgs.gov/Landsat8_Using_Product.php (accessed in Sep, 2013)

Vermote, E. F., Tanre, D., Deuze, J. L., Herman, M., & Morcette, J. J. (1997). Second simulation of the satellite signal in the solar spectrum, 6S: An overview. *IEEE Geoscience and Remote Sensing*, *35*, 675–686.

Wang, J. J., Lu, X. X., Liew, S.C., & Zhou, Y. (2009). Retrieval of suspended sediment concentrations in large turbid rivers using Landsat ETM+: An example from the Yangtze River, China. *Earth Surface Processes and Landforms*, *34*, 1082–1092.

Wang, M., & Shi, W. (2007). The NIR-SWIR combined atmospheric correction approach for MODIS ocean color data processing. *Optics Express*, *15*, 15722–15733.

Wang, Y., Xia, H., Fu, J., & Sheng, G. (2004). Water quality change in reservoirs of Shenzhen, China: Detection using LANDSAT/TM data. *Science of the Total Environment*, *328*, 195–206.